applied sciences

MDPI

Article

Synthesis of High-Precision Sub-Micron $CaCO_3$ Anticancer Drug Carriers from Coral Remains

Pin-Han Chen [1], Wei-Sheng Chen [1,2,*], Szu-An Chen [1] and Wei-Chung Chen [1]

[1] Department of Resources Engineering, National Cheng Kung University, Tainan City 701401, Taiwan; n48111017@gs.ncku.edu.tw (P.-H.C.); n46114158@gs.ncku.edu.tw (S.-A.C.); n48111033@gs.ncku.edu.tw (W.-C.C.)
[2] Hierarchical Green-Energy Materials (Hi-GEM) Research Center, National Cheng Kung University, Tainan City 701401, Taiwan
* Correspondence: kenchen@mail.ncku.edu.tw

Abstract: Calcium carbonate ($CaCO_3$) particles have attracted increasing attention as a promising material for drug delivery systems. In this study, coral remains were utilized as a raw material for a novel drug carrier. A series of pre-treatment and parameter experiments were conducted to synthesize sub-micron spherical $CaCO_3$ particles. The $CaCO_3$ particles exhibited uniform size distribution, with the minimum mean size being only 344 nm. The effects on the $CaCO_3$ crystal phases and particle sizes were also discussed in this study. Drug loading experiments were also conducted to assess the feasibility of the $CaCO_3$ drug carrier. We loaded TRITC-Dextran into $CaCO_3$ particles for the simulation experiments. The loading capacity reached up to 9.6 wt.%, which was as high as common drug carriers such as liposomes. In this study, we aimed not only to tackle the local environmental issues caused by coral remains, but also to synthesize a suitable drug carrier for cancer therapy using the outstanding properties and low cost of $CaCO_3$.

Keywords: waste recovery; precipitated calcium carbonate; spherical vaterite; drug carrier; drug delivery system

Citation: Chen, P.-H.; Chen, W.-S.; Chen, S.-A.; Chen, W.-C. Synthesis of High-Precision Sub-Micron $CaCO_3$ Anticancer Drug Carriers from Coral Remains. *Appl. Sci.* **2024**, *14*, 1336. https://doi.org/10.3390/app14041336

Academic Editor: María Ángeles Cancela Carral

Received: 23 December 2023
Revised: 26 January 2024
Accepted: 31 January 2024
Published: 6 February 2024

1. Introduction

Environmental degradation and disease are the two major challenges of this century. This study explores a novel solution to deal these issues by addressing the accumulated coral remains in Taiwan and their potential application in cancer drug development, one of the leading causes of death worldwide. Coral remains are composed of coral fragments resulting from weathering, waves, or trampling. It is a unique environmental issue in Taiwan. Despite coral remains being non-toxic and harmless, the accumulation of coral causes lots of problems along the coast in Penghu, one of the counties in Taiwan. Coral remains accumulating along the coast lead to a reduction in marine life living spaces and the obstruction of fishing routes, impacting fishermen's livelihoods. The local government tried to dredge the coral remains and place them onto the beach. Unfortunately, the resulting odor and damage to the landscape continued to constitute serious problems. Coral remains consist of $CaCO_3$, which is known as a safe, cheap, and clean industrial mineral. Compared to oyster shells, coral remains do not require a significant amount of time for washing and cleaning, making them an ideal material for this study.

Cancer is one of the most critical issues around the world. The International Agency for Research on Cancer (IARC) and the Union for International Cancer Control (UICC) reported nearly 19.3 million cancer cases, with the death toll reaching up to 10 million in 2020 [1]. Moreover, cancer has been the leading cause of death in Taiwan since 1982, accounting for 28.98% of all deaths in 2020, totaling 50,161 people [2]. Due to the toxicity of cancer drugs, the precision of drug delivery is a significant feature in curing cancers. Therefore, a growing amount of research is committed to loading drugs into unique containers to improve the

precision of drug delivery, i.e., drug carriers [3,4]. There is currently a variety of drug carriers such as liposomes, solid lipid nanoparticles, gold nanoparticles, etc. However, they still have some critical problems that must be dealt with, e.g., bio-toxicity, aggregation, and high cost.

$CaCO_3$ is a promising and novel material for drug carriers. It possesses several properties, including high biocompatibility, substantial drug loading capacity, pH sensitivity, low cost, and the capability to carry multiple drugs simultaneously [5–9]. It is widely used as an industrial mineral [10–19] and a raw material for pharmaceutical products [20,21]. $CaCO_3$ has been utilized as a carrier to deliver proteins and genes [22]. Therefore, the public acceptability of $CaCO_3$ is better than that of other materials. Moreover, according to the report from Vikulina et al. [23], $CaCO_3$ costs only 0.2–0.4 USD/g, which is significantly lower than the 100 USD/g cost of liposomes.

$CaCO_3$ is widely used in industry as a filler. It can not only lower the cost but also improve the properties of products [24,25]. $CaCO_3$ has three major anhydrous phases: calcite, aragonite, and vaterite [26,27]. Calcite is the most stable phase among them, followed by aragonite and vaterite [28–31]. Vaterite is the least stable but the most promising phase for a drug carrier due to its high porosity, large surface, and higher solubility. Vaterite will gradually dissolve and recrystallize into calcite in water, which is an imperative mechanism for drugs to be released from vaterite (Figure 1). Owing to the instability of vaterite, the synthesizing process must be studied to control the morphology, particle size, and purity of it. To manipulate the morphologies and particle sizes of $CaCO_3$, the addition of additives is the general approach for achieving this [32–38]. Parakhonskiy et al. reported that polyol can inhibit $CaCO_3$ from growing into other phases [39]. Thus, we used ethylene glycol (EG) as an additive to maintain the vaterite phase [40–42]. EG can also control the particle size of vaterite, as studies have indicated that cancer cells take up molecules smaller than 600 nm selectively due to the enhanced permeability and retention effect (EPR effect) [43].

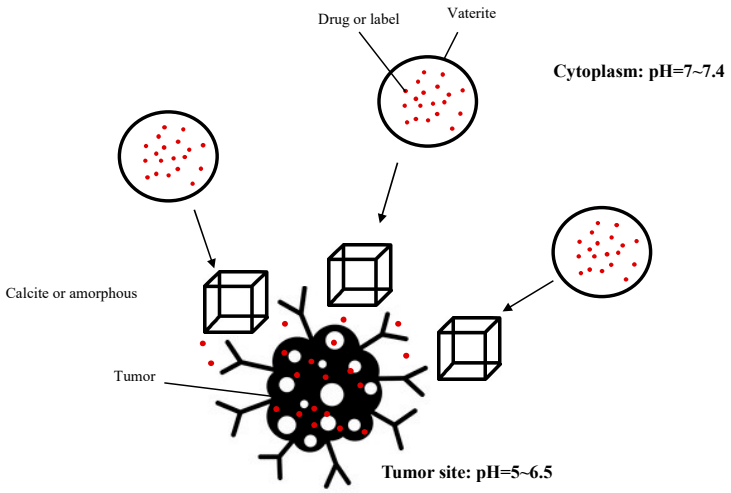

Figure 1. Schematic illustration of drug release from a $CaCO_3$ drug carrier.

2. Materials and Methods

2.1. Materials

Coral remains from Penghu coastal accumulations and dredging operations were used as the raw material for this study. Coral remains were collected by scholars from Penghu University of Science and Technology. The dredging operations were carried out by the Penghu government. The coral remains were dredged and placed along the coast so that we could easily collect them with permission from the government.

2.2. Pretreatment and Characteristic Analysis of Coral Remains

Coral remains underwent washing, hydrogen peroxide immersing, drying, and grinding, followed by 60-mesh sieving. For elemental analysis, the sample was calcined at 1000 °C for 4 h, then dissolved in a mixture of aqua regia and hydrofluoric acid (HF) in the ratio of 9:1. Following these procedures, the solution was analyzed using Inductively Coupled Plasma Optical Emission Spectrometry (ICP-OES, Avio 200 Manx, PerkinElmer, Waltham, MA, USA).

2.3. Purification of Coral Remains and Preparation of $CaCl_2$

Purification began with the calcination of coral remains at 1000 °C to decompose them into CaO, which was then dissolved in water to form $Ca(OH)_2$. This step was followed by a reaction with CO_2, resulting in the precipitation of $CaCO_3$. The calcination was carried out in a tube furnace under different atmospheres (air, N_2, and CO_2) to study the decomposition rate of $CaCO_3$ in varying conditions. The calcination temperatures in air and N_2 were set between 700 °C and 1200 °C. In the case of CO_2, temperatures ranged from 500 °C to 1000 °C due to no significant improvement observed beyond 700 °C, prompting the extension down to 500 °C. The decomposition rates of $CaCO_3$ were calculated using the following equation (Equation (1)), where x represents the decomposition rate and 44 is the molecular weight of CO_2. The purity of the resulting $CaCO_3$ was confirmed using ICP-OES, and it was subsequently reacted with HCl to produce $CaCl_2$, as shown in the following equations (Equations (2) and (3)):

$$x = (\text{mass of } CaCO_3 - \text{mass of CaO})/44 \quad (1)$$

$$CaCO_{3(s)} + 2HCl_{(aq)} \rightarrow CaCl_{2(aq)} + CO_{2(g)} + H_2O_{(l)} \quad (2)$$

$$CaCl_{2(aq)} \xrightarrow{\Delta} CaCl_{2(s)} \quad (3)$$

2.4. Exploration of Optimal Parameters for the Synthesis of Vaterite

Solutions with different concentrations of $CaCl_2$ and Na_2CO_3 were prepared and injected into EG in specific ratios. Further steps included centrifugation, washing, and drying at 60 °C for 2 h. Given the complex reaction mechanism involved in vaterite formation, a thorough investigation was conducted to gain a comprehensive understanding of its reaction mechanisms and characteristics. This involved exploring a range of parameters, such as the concentration of EG, stirring speed, total reaction time, initial salt concentration, reaction volume, and the adding order of $CaCl_2$ and Na_2CO_3. The particle size and crystal phase variations of $CaCO_3$ under these different conditions were carefully observed to identify the optimal synthesis parameters. For examining the vaterite crystal structure, Scanning Electron Microscopy (SEM, Hitachi SU-1510, Tokyo, Japan) was utilized, with the samples being coated with a palladium (Pd) layer. The particle size distribution was quantified using ImageJ Version 1.54h, with a sample size of $N \geq 150$ particles per sample.

2.4.1. Adding Order of the Salts

$CaCO_3$ was synthesized using the precipitation method, involving $CaCl_2$ and Na_2CO_3. We found that the order in which these salts are added plays a critical role, a parameter not extensively discussed in the existing literature. Altering the sequence of adding $CaCl_2$ and Na_2CO_3 resulted in significant variations in the crystal forms and particle sizes of the synthesized $CaCO_3$. Therefore, the impact of the adding order of these salts was emphasized in this study.

2.4.2. Stirring Speed

This section examined the effect of various stirring speeds (400, 600, 800, 1000, and 1150 rpm) on the particle size of $CaCO_3$.

2.4.3. EG Concentration

Ethylene glycol (EG) played a critical role in this study due to its high viscosity, which decelerates ion diffusion and inhibits the growth of $CaCO_3$. We investigated various EG concentrations, including 0%, 25%, 50%, and 85%, to determine their impact on the synthesis of $CaCO_3$.

2.4.4. Reaction Time

The presence of EG is known to mitigate the reaction speed. We explored how varying reaction times influence the diversity of $CaCO_3$ formations. In this study, time intervals of 1 min, 30 min, 60 min, 180 min, and 1440 min (1 day) were examined to determine the optimal reaction duration.

2.4.5. Initial Salt Concentration

Nucleation theory suggests that the initial salt concentration can impact the nucleation rate, consequently affecting the particle size. This study varied the initial concentrations of $CaCl_2$ and Na_2CO_3 to observe the resulting changes in $CaCO_3$ and to validate the alignment of our findings with the nucleation theory.

2.4.6. Total Reaction Volume

This investigation explored the effects of different total reaction volumes, including the combined volumes of salt solutions and EG. Contrasting with the common practice in the literature, which typically synthesizes $CaCO_3$ using drug carriers around 100 mL, we extended this range to include volumes of 4 mL, 40 mL, 120 mL, and 400 mL to investigate the formation and characteristic of $CaCO_3$.

2.5. Drug Loading Simulation Experiment

The fluorescently labeled drug Tetramethylrhodamine Isothiocyanate–Dextran (TRITC-Dextran) was utilized for loading into $CaCO_3$ carriers, and the loading capacity (LC) was subsequently calculated after drug loading. For LC calculation, an indirect method [44] was employed. This method involves analyzing the concentration of the drug in the supernatant collected after centrifugation the drug-loaded carrier. The LC is then estimated by deducting the drug concentration in the supernatant from the initial drug concentration. The concentration of TRITC-Dextran was maintained at 10 mg/mL in this study. We analyzed the collected supernatant using a Fluorescence Spectrophotometer (Fluorescence Spectrophotometer, Hitachi High-Tech F-7000, Hitachi High-Technologies Corporation, Tokyo, Japan). The drug-loaded carriers were examined under a confocal microscope (Confocal Microscope, Carl Zeiss LSM780, Carl Zeiss AG, Oberkochen, Germany) to assess the amount of TRITC-Dextran loaded into the $CaCO_3$ particles. An excitation wavelength of $\lambda = 530$ nm was utilized in this study. The drug concentration in the supernatant was calculated using the following equation (Equation (4)):

$$F = P_0(2.3\varepsilon bc)Q_f k \quad (4)$$

where F represents the intensity of fluorescence, P_0 is the incident power, ε is the molar absorptivity, b is the path length, c is the concentration, Q_f is the quantum efficiency, and k is the ratio of photons measured to photons emitted. Typically, P_0, ε, b, Q_f, and k are constant, making the concentration in the supernatant directly proportional to the fluorescence intensity F.

3. Result and Discussion

3.1. Characteristic Analysis of Coral Remains

Tables 1 and 2 present the elemental composition of the raw and purified coral remains, as determined by ICP-OES. The raw coral remains primarily consisted of elements such as Ca, Mg, and Si, with no detectable levels of Pb and Cd. After purification, the purity of CaO

significantly increased from 92.95% to 99.965%, indicating the effective removal of most impurities. This aligns with the 2023 Republic of China National Regulations Database standards for $CaCO_3$ (§ 07014) [45], particularly for use in food and nutrition applications. These standards require a $CaCO_3$ content of over 98%, less than 0.2% hydrochloric acid insoluble residue, and lead levels below 10 ppm. Consequently, the purified coral remains qualify as food-grade additive.

Table 1. Composition of raw coral remains.

Ingredient	Proportion
CaO	92.95123%
MgO	3.67358%
MnO_2	0.00300%
Fe_2O_3	0.47249%
SiO_2	2.13416%
Al_2O_3	0.77554%
PbO	N/A
CdO	N/A

Table 2. Composition of purified coral remains.

Ingredient	Proportion
CaO	99.96482%
MgO	0.00158%
MnO_2	0.00006%
Fe_2O_3	0.00035%
SiO_2	0.01910%
Al_2O_3	0.01409%
PbO	N/A
CdO	N/A

3.2. Purification of Coral Remains and Preparation of $CaCl_2$

The calcination efficiency of coral remains under different atmospheres is shown in Figure 2a–c. The decomposition rate of $CaCO_3$ to CaO in an N_2 atmosphere showed a significant increase, achieving complete reaction in just 5 min at 800 °C, compared to the 15 min required at 900 °C in an air atmosphere. In a CO_2 atmosphere, the decomposition rate experienced a slight increase and stabilized after reaching 700 °C. However, the decomposition rate plateaued at 13%, even after extending the duration to 30 min at 1000 °C. This could be attributed to the Le Châtelier's principle, where the high partial pressure of CO_2 generated during the calcination process inhibited further decomposition. Conversely, in the N_2 atmosphere, the inert gas was continuously removed from the system with the simultaneous introduction of N_2, facilitating a decomposition rate reaching 100% in just 5 min at 800 °C. These findings verified the theory that CO_2 partial pressure significantly affects the efficiency of decomposition. Therefore, based on the results, an N_2 atmosphere was determined to be the optimal condition for calcination.

3.3. Exploration of Optimal Parameters for the Synthesis of Vaterite

3.3.1. Adding Order of the Salts

This step explored the effects of the different adding orders of the salts on the synthesis of $CaCO_3$, with operational parameters detailed in Table 3. The SEM results depicted in Figure 3 reveal that adding $CaCl_2$ before Na_2CO_3 significantly affects the particle size, resulting in a more uniform distribution compared to adding Na_2CO_3 before $CaCl_2$. The average particle size for $CaCl_2$-first was found to be 423 nm, compared to 869 nm for Na_2CO_3-first. Consequently, $CaCl_2$-first was chosen as the optimal parameter for subsequent reactions.

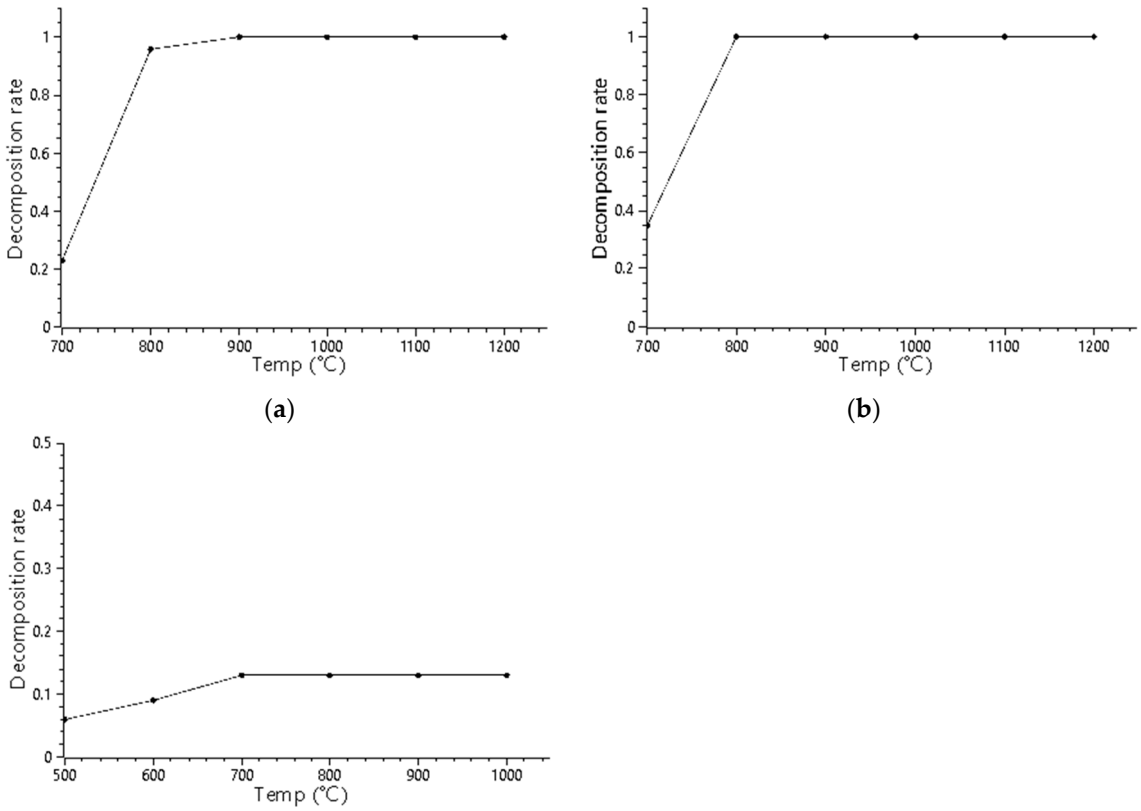

Figure 2. The decomposition rate under different atmospheres: (**a**) air; (**b**) N_2; (**c**) CO_2.

Table 3. Parameters for reaction base experiment.

Factors	Parameters
Adding Order	$CaCl_2$-first, Na_2CO_3-first
Stirring Speed (rpm)	1000 rpm
Concentration of EG	85%
Reaction Time (min)	60
$CaCl_2/Na_2CO_3$ (M)	1 M/0.1 M
Reaction Volume (mL)	4

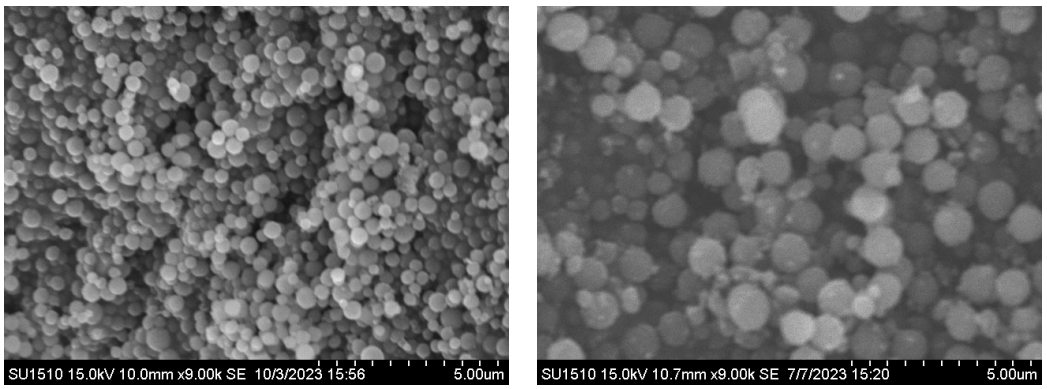

Figure 3. Particle size distribution of $CaCO_3$ synthesized with two different adding orders of the salts: (**a**) $CaCl_2$-first (**b**) Na_2CO_3-first.

3.3.2. Stirring Speed

This step investigated the impact of different stirring speeds on the particle size of $CaCO_3$, with the operational parameter outlined in Table 4. As shown in Figure 4a, an increase in stirring speed corresponded with a reduction in the average particle size of $CaCO_3$. Notably, at 400 rpm, the formation of numerous calcite particles and some particle aggregation was observed (Figure 4b); as a result, the data obtained from this speed setting was deemed unsuitable in our discussion. At a speed of 1150 rpm, the particle size was reduced to an average of 364 nm, making it the optimal parameter.

Table 4. Parameters for stirring speed experiment.

Factors	Parameters
Adding Order	$CaCl_2$-first
Stirring Speed (rpm)	400, 600, 800, 1000, 1150
Concentration of EG	85%
Reaction Time (min)	60
$CaCl_2/Na_2CO_3$ (M)	1 M/0.1 M
Reaction Volume (mL)	4

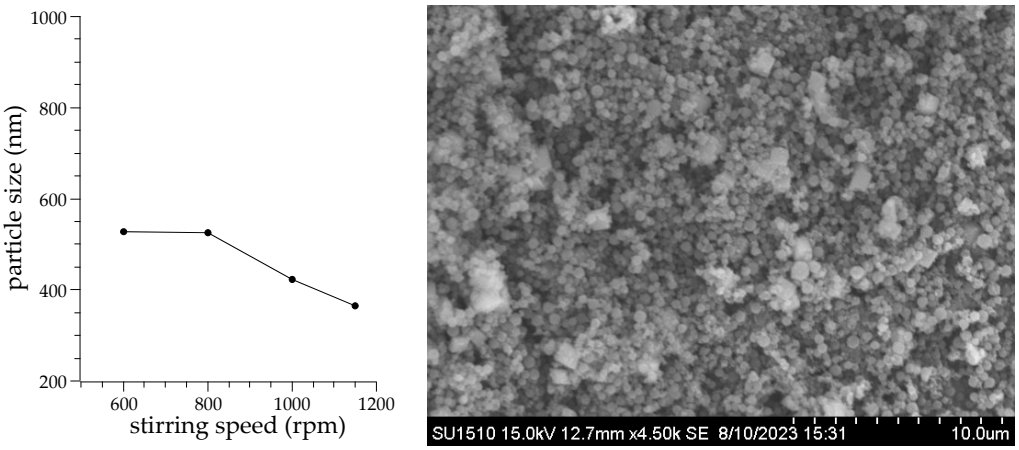

(**a**) (**b**)

Figure 4. (**a**) Average particle size as a function of different stirring speeds. (**b**) SEM image of $CaCO_3$ with 400 rpm stirring speed.

3.3.3. EG Concentration

This step examined the effect of different EG concentrations on the particle size and crystal growth of $CaCO_3$, with operational parameters detailed in Table 5. As demonstrated in Figure 5a,b, $CaCO_3$ samples with an EG concentration of less than 50% tended to form calcite-like crystals, which was attributed to an overreaction. Conversely, increasing the EG concentration above 50% gradually suppressed the growth rate of $CaCO_3$, favoring the formation of complete vaterite structures. This is evident in particle size and distribution observed at higher EG concentrations, which were more favorable compared to those observed at 50% or lower, as shown in Figure 5c,d. The mean particle sizes at 50% and 85% EG concentrations were 1038 nm and 475 nm, respectively. Therefore, the optimal EG concentration was determined to be 85%.

Table 5. Parameters for EG concentration experiment.

Factors	Parameters
Adding Order	$CaCl_2$-first
Stirring Speed (rpm)	1000
Concentration of EG	0%, 25%, 50%, 85%
Reaction Time (min)	60
$CaCl_2/Na_2CO_3$ (M)	1 M/0.33 M
Reaction Volume (mL)	4

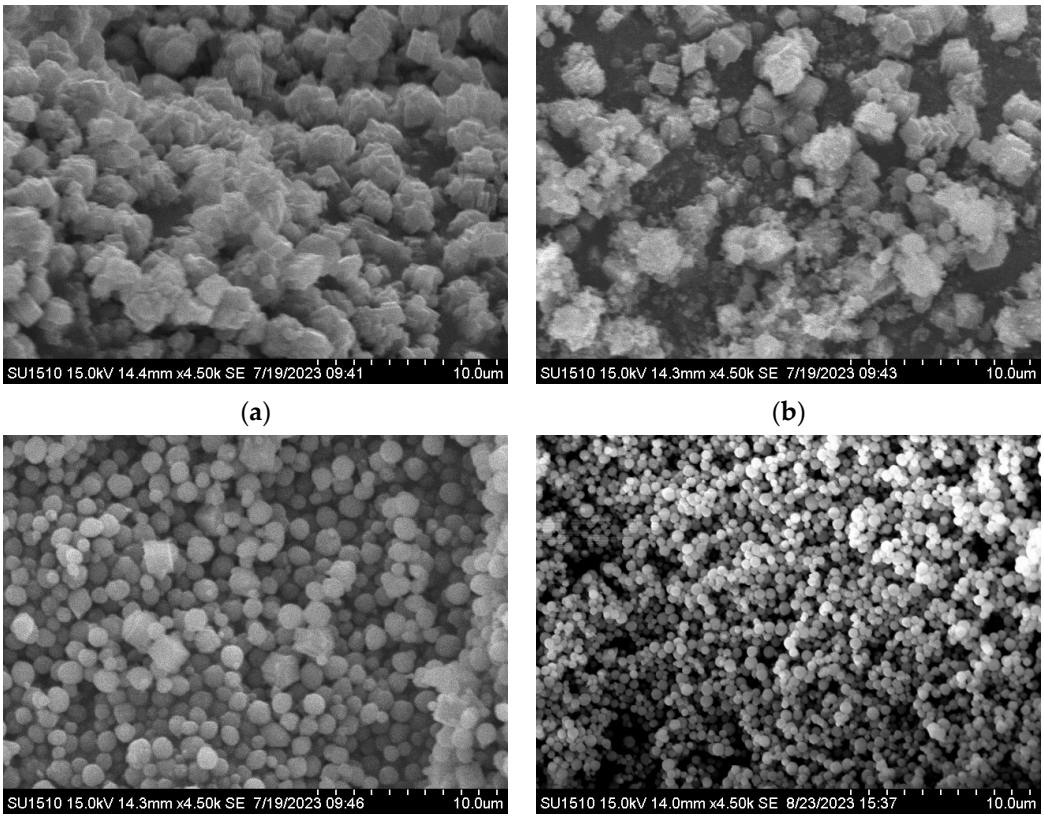

Figure 5. SEM images of $CaCO_3$ synthesized with insufficient concentrations of EG: (**a**) 0%; (**b**) 25%; (**c**) 50%; (**d**) 85%.

3.3.4. Reaction Time

This step explored the effect of different reaction times on the formation of vaterite crystals, with operational parameters outlined in Table 6. SEM analysis (Figure 6a–e) indicated that the optimal vaterite crystal phase and particle size distribution were achieved at a reaction time of 1 h (Figure 6c). It was observed that extending the reaction led to an increase in particle size. This increase might be attributed to the continuous formation of $CaCO_3$ at nucleation sites, facilitated by the interaction of Ca^{2+} and CO_3^{2-} ions. Notably, for reaction times shorter than one hour (Figure 6a,b), a clear presence of both calcite and larger vaterite particles was observed, with instances where calcite appeared embedded within vaterite. This suggests that the complete formation of vaterite might undergo a process of continuous decomposition and recrystallization, aligning with findings from Zhang et al. [46]. Therefore, a duration of 60 min was determined to be the optimal reaction time.

Table 6. Parameters for reaction time experiment.

Factors	Parameters
Adding Order	$CaCl_2$-first
Stirring Speed (rpm)	1000
Concentration of EG	85%
Reaction Time (min)	5, 30, 60, 180, 1440
$CaCl_2/Na_2CO_3$ (M)	1 M/0.1 M
Reaction Volume (mL)	4

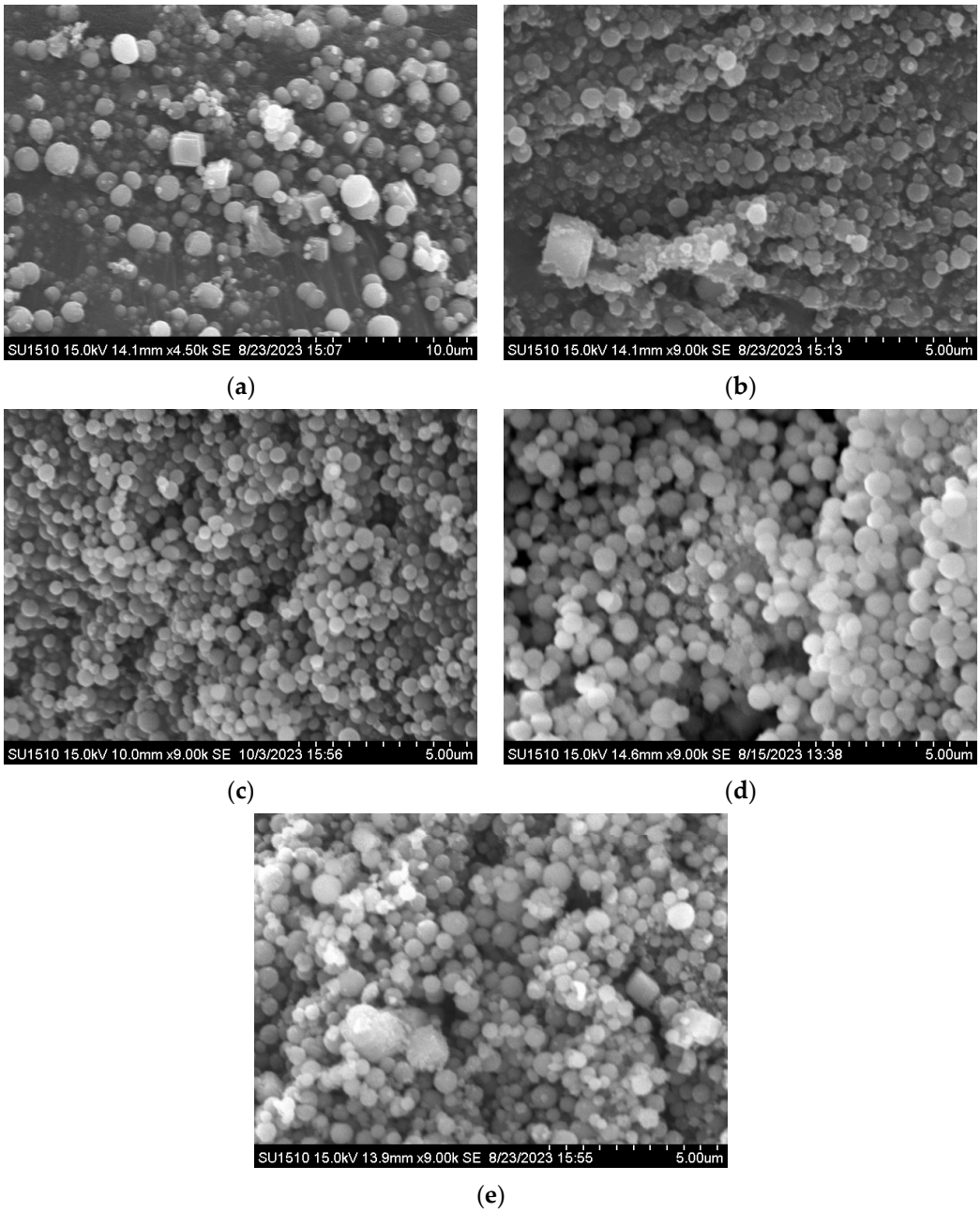

Figure 6. SEM images of $CaCO_3$ synthesized with varying reaction times: (**a**) 5 min; (**b**) 30 min; (**c**) 60 min; (**d**) 180 min; (**e**) 1440 min.

3.3.5. Initial Salt Concentration

Salt concentration affects the nucleation rate, which consequently influences the particle size. In this step, the effect of varying Na_2CO_3 concentrations on the particle size of $CaCO_3$ was examined, with operational parameters detailed in Table 7. Results from Figure 7a–e indicate that the particle size of $CaCO_3$ increases together with a rise in the concentration of Na_2CO_3, presenting an opposite trend from the classic nucleation theory [47]. Notably, the smallest particle size was 344 nm at a Na_2CO_3 concentration of 0.05 M, aligning with the hypothesis proposed by Trushina et al. [40].

Table 7. Parameters for initial salt concentration.

Factors	Parameters
Adding Order	$CaCl_2$-first
Stirring Speed (rpm)	1000
Concentration of EG	85%
Reaction Time (min)	60
$CaCl_2/Na_2CO_3$ (M)	1 M/0.05 M, 0.1 M, 0.33 M, 0.5 M, 1 M
Reaction Volume (mL)	4

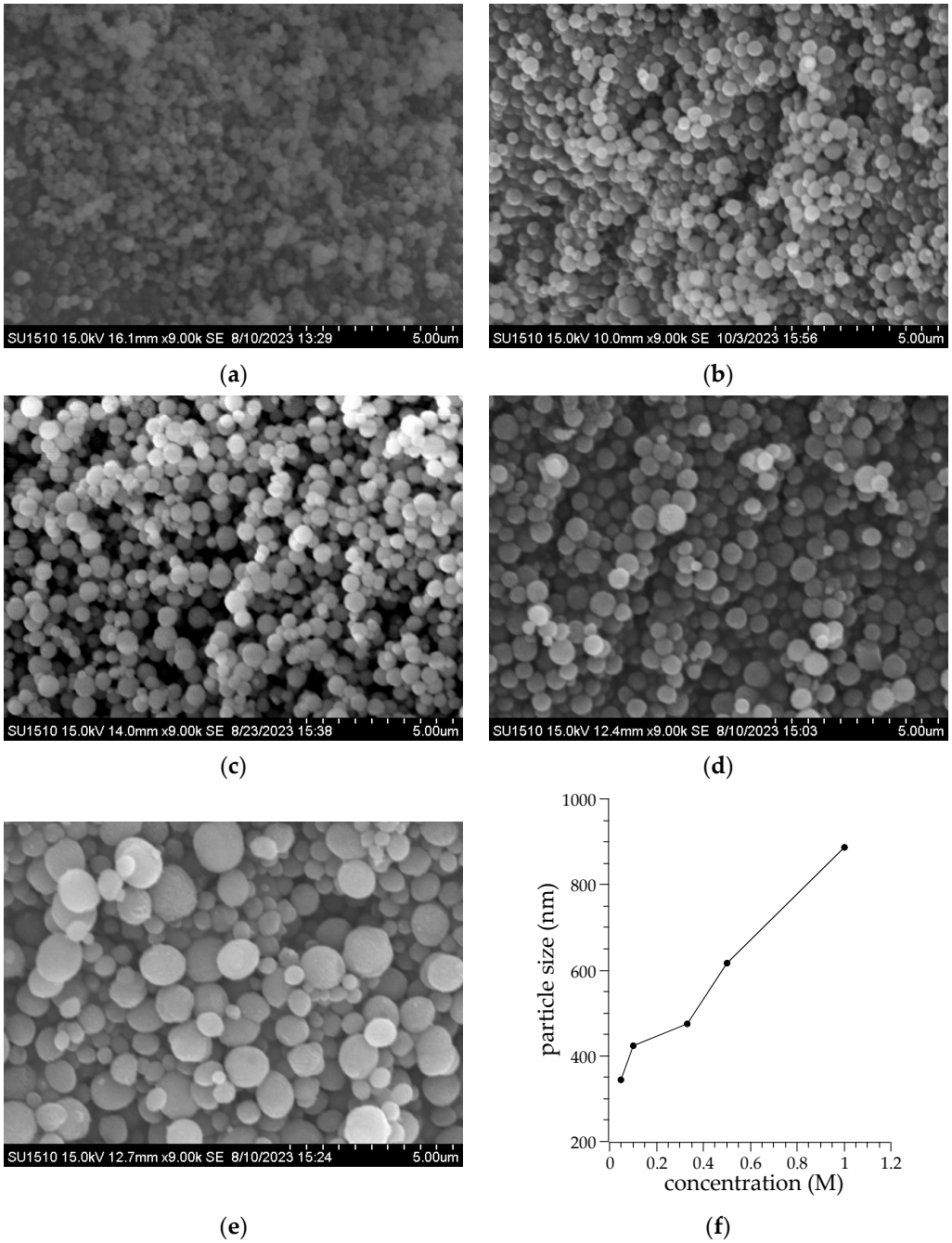

Figure 7. SEM images of $CaCO_3$ synthesized with varying initial salt concentrations of Na_2CO_3: (**a**) 0.05 M; (**b**) 0.1 M; (**c**) 0.33 M; (**d**) 0.5 M; (**e**) 1 M; (**f**) average particle size as a function of different initial salt concentrations.

However, this study yielded $CaCO_3$ particles with an average size of 423 nm at 0.1 M Na_2CO_3, contrasting with findings from Trushina et al., who observed the smallest particles at 700 nm under similar conditions [40]. This phenomenon may be attributed to the interaction between the functional groups of EG and Ca^{2+} ions. The former, carrying opposite electrical charges, possibly facilitates the occupancy of Ca^{2+} ions at EG's nucleation sites. Upon adding Na_2CO_3, the CO_3^{2-} ions were prompted to react with Ca^{2+} ions at these nucleation sites, leading to the formation of $CaCO_3$. Based on the experimental results, the optimal initial salt concentration was determined to be $CaCl_2$:Na_2CO_3 = 1 M:0.05 M.

3.3.6. Total Reaction Volume

This step investigated the impact of total reaction volumes on the particle size of $CaCO_3$, with operational parameters detailed in Table 8. Observations from Figure 8a–d reveal that the particle size of vaterite increased with the increment of reaction volume. Notably, the particle size of vaterite in a 400 mL solution reached 1002 nm. Moreover, the presence of calcite phase was observed in reactions conducted with 400 mL (Figure 8d). This phenomenon indicates that the total reaction volume has a noticeable impact not only on the particle size, but also on the crystal morphology of the products. Based on the experimental results, the optimal reaction volume was determined to be 4 mL for achieving the desired particle size and crystal structure.

Table 8. Parameters for total reaction volume experiment.

Factors	Parameters
Adding Order	$CaCl_2$-first
Stirring Speed (rpm)	1000
Concentration of EG	85%
Reaction Time (min)	60
$CaCl_2/Na_2CO_3$ (M)	1 M/0.1 M
Reaction Volume (mL)	4, 40, 120, 400

3.4. Summary of Optimal Parameters for Drug Carrier Synthesis

The following table (Table 9) shows a series of optimal parameters identified from the experiments.

Table 9. Optimal parameters for $CaCO_3$ synthesis.

Factors	Parameters
Adding Order	$CaCl_2$-first
Stirring Speed (rpm)	1150
Concentration of EG	85%
Reaction Time (min)	60
$CaCl_2/Na_2CO_3$ (M)	1 M/0.05 M
Reaction Volume (mL)	4

3.5. Drug Loading Simulation Experiment

The co-precipitation method was employed to synthesize calcium carbonate ($CaCO_3$) drug carriers, incorporating the fluorescently labeled drug TRITC-Dextran directly into the $CaCO_3$ synthesis process. The drug loading results of TRITC-Dextran (Figure 9b) shows that nearly all $CaCO_3$ particles emitted fluorescence signals, indicating effective drug incorporation into the carrier matrix. The results of the loading capacity (LC), which is calculated by Equation (4), reveal that the LC for the $CaCO_3$ drug carrier was 9.6 wt.%, compared with the LC of 10.3 wt.% achieved by Taman et al. [48] using liposomes for Gemcitabine (Gem) delivery. Typically, the LCs for liposome-based drug delivery systems range between 5 and 10 wt.%. In contrast, Donatan et al. [49], who utilized an adsorption method for loading TRITC-Dextran onto $CaCO_3$, reported an LC of less than 1 wt.%;

similarly, Parakhonskiy et al. [6], employing the adsorption method, achieved a maximum LC of only 0.01 wt.%. These comparisons highlight the efficiency of the co-precipitation method and its promising capability for drug carrier fabrication using $CaCO_3$.

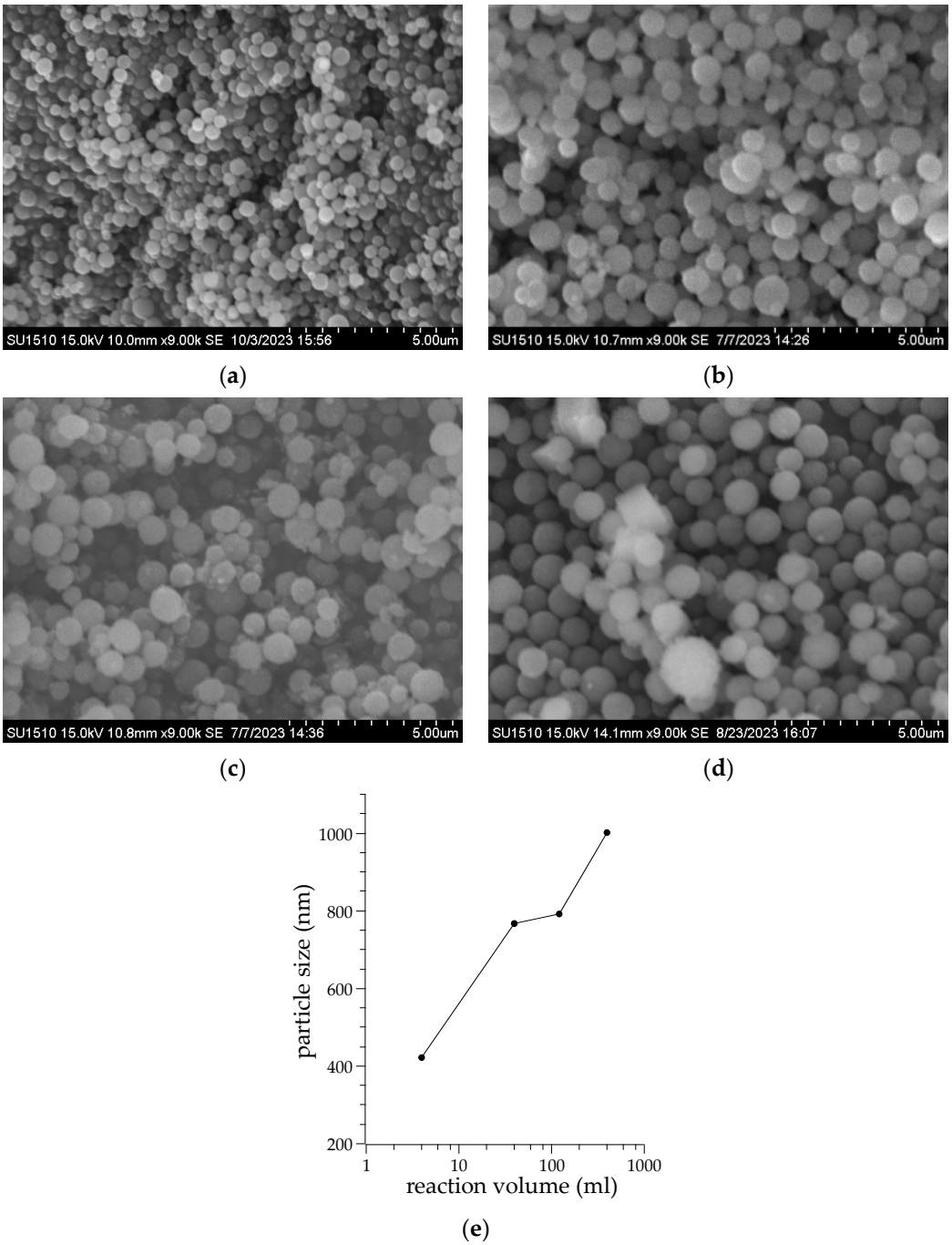

Figure 8. SEM images of $CaCO_3$ synthesized with varying total reaction volumes: (**a**) 4 mL; (**b**) 40 mL; (**c**) 120 mL; (**d**) 400 mL; (**e**) average particle size as a function of different reaction volumes.

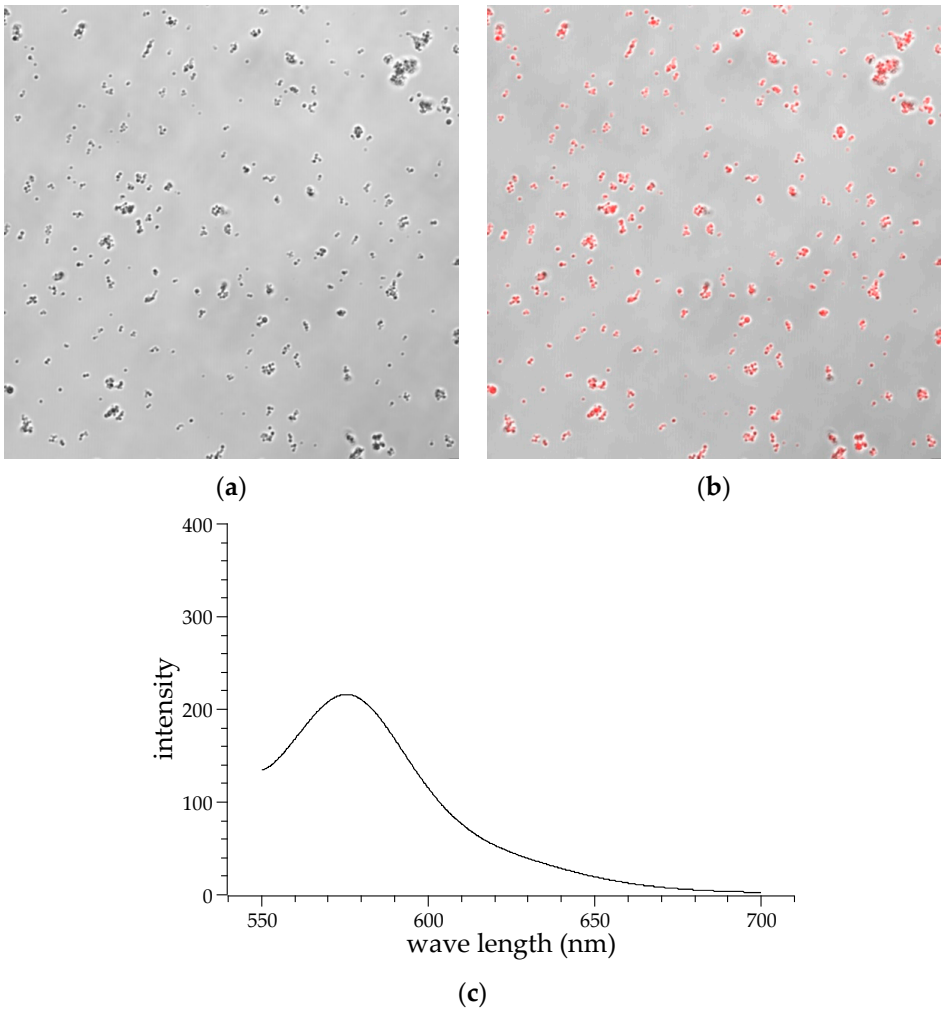

Figure 9. Loading result of TRITC-Dextran: (**a**) synthesized calcium carbonate ($CaCO_3$) only; (**b**) with the fluorescently labeled (red signals on the particles) drug TRITC-Dextran; (**c**) the fluorescence spectrum of the supernatant.

4. Conclusions

Compared to other calcium-rich biogenic wastes such as oyster and clam shells, coral remains at present to be a cleaner and more easily collected alternative. This study, initiated from a circular economy perspective, investigated the potential of repurposing coral remains, a topic typically associated with environmental challenges, into a valuable raw material for better use. The major composition of coral remains is $CaCO_3$, a common raw material in industrial and pharmaceutical products. In this study, coral remains could meet the industrial standards for $CaCO_3$ undergoing a series of purification and modification processes. Vaterite, one of the crystal phases of $CaCO_3$, demonstrated excellent physicochemical properties, making it a promising material for anticancer drug carriers. The conclusions drawn from the experiments are as follows:

1. The composition analysis of coral remains showed the absence of heavy metals such as Pd and Cd, both of which are of most concern in food and pharmaceutical products, indicating their suitability as raw materials for these industries.
2. The efficient conversion of $CaCO_3$ to CaO in an N_2 atmosphere at 800 °C within just 5 min demonstrates a significant enhancement in process efficiency, potentially reducing both time and cost.
3. The whiteness level of purified $CaCO_3$ reached 95%, surpassing many industrial standards (93%), making it suitable for industrial applications.

4. The synthesized vaterite possesses several desirable drug carrier properties such as spherical morphology, small particle size, high porosity, pH sensitivity, and biocompatibility. Given its widespread use in the food and pharmaceutical industries, $CaCO_3$ has shown to be a superior option for anticancer drug delivery compared to other drug carriers such as mesoporous silica nanoparticles and gold nanoparticles.
5. The effective utilization of the EPR effect for targeting cancer cell necessitates particle sizes below 600 nm. Smaller particles are more efficient in penetrating cell membranes and also positively impact the drug loading capacity, a crucial factor of the efficiency of $CaCO_3$ as a drug carrier. While typical reproducibility of vaterite particle size range from 4 to 6 μm [40,50,51], our study successfully synthesized drug carriers with an average size of 344 nm, and some even smaller than 200 nm.
6. During $CaCO_3$ synthesis, the involvement of EG necessitated sufficient time to form a complete vaterite crystal. Insufficient time resulted in the formation of either amorphous phases or incomplete calcite crystals.
7. Given the high costs associated with cancer drug production and the expensive, intricately synthesized carriers typically used for their delivery, the overall price of anticancer drug carriers remains notably high. $CaCO_3$, in contrast, is a widely available, cost-effective, and stable material. Its application as a drug carrier could significantly reduce costs while maintaining excellent biocompatibility and precision in drug delivery. This approach not only provides a solution to the high expenses involved in synthesizing drug carriers, but also tackles environmental concerns related to coral remains, offering a dual advantage.

Author Contributions: Conceptualization, S.-A.C. and W.-S.C.; methodology, W.-C.C.; software, S.-A.C.; validation, S.-A.C. and W.-C.C.; formal analysis, S.-A.C.; investigation, S.-A.C.; resources, S.-A.C.; data curation, S.-A.C.; writing—original draft preparation, P.-H.C.; writing—review and editing, P.-H.C.; visualization, P.-H.C.; supervision, W.-S.C.; project administration, S.-A.C.; funding acquisition, S.-A.C. All authors have read and agreed to the published version of the manuscript.

Funding: This research was funded by the National Science and Technology Council, Taiwan, under grant NSTC 111-2621-M-006-007.

Institutional Review Board Statement: Not applicable.

Informed Consent Statement: Not applicable.

Data Availability Statement: The data presented in this study are available in article.

Acknowledgments: The authors wish to extend their sincere gratitude to the members of the laboratory team for their invaluable administrative assistance throughout this study.

Conflicts of Interest: The authors declare no conflicts of interest.

References

1. Chhikara, B.S.; Parang, K. Global Cancer Statistics 2022: The trends projection analysis. *Chem. Biol. Lett.* **2023**, *10*, 45.
2. Health Promotion Administration, Ministry of Health and Welfare. Cancer Registry Annual Report, 2020 Taiwan; 2020; pp. 1–669. Available online: https://www.hpa.gov.tw/Pages/Detail.aspx (accessed on 20 January 2024).
3. Hami, Z. A brief review on advantages of nano-based drug delivery systems. *Ann. Mil. Health Sci. Res.* **2021**, *19*, e112274. [CrossRef]
4. Singh, S. Nanomedicine–nanoscale drugs and delivery systems. *J. Nanosci. Nanotechnol.* **2010**, *10*, 7906–7918. [CrossRef] [PubMed]
5. Zhao, Q.; Cheng, N.; Sun, X.; Yan, L.; Li, W. The application of nanomedicine in clinical settings. *Front. Bioeng. Biotechnol.* **2023**, *11*, 1219054. [CrossRef] [PubMed]
6. Parakhonskiy, B.V.; Yashchenok, A.M.; Donatan, S.; Volodkin, D.V.; Tessarolo, F.; Antolini, R.; Möhwald, H.; Skirtach, A.G. Macromolecule Loading into Spherical, Elliptical, Star—Like and Cubic Calcium Carbonate Carriers. *ChemPhysChem* **2014**, *15*, 2817–2822. [CrossRef] [PubMed]
7. Tannock, I.F.; Rotin, D. Acid pH in tumors and its potential for therapeutic exploitation. *Cancer Res.* **1989**, *49*, 4373–4384. [PubMed]
8. Svenskaya, Y.; Parakhonskiy, B.; Haase, A.; Atkin, V.; Lukyanets, E.; Gorin, D.; Antolini, R. Anticancer drug delivery system based on calcium carbonate particles loaded with a photosensitizer. *Biophys. Chem.* **2013**, *182*, 11–15. [CrossRef] [PubMed]

9. Wu, J.-L.; Wang, C.-Q.; Zhuo, R.-X.; Cheng, S.-X. Multi-drug delivery system based on alginate/calcium carbonate hybrid nanoparticles for combination chemotherapy. *Colloids Surf. B Biointerfaces* **2014**, *123*, 498–505. [CrossRef]
10. Jimoh, O.A.; Ariffin, K.S.; Hussin, H.B.; Temitope, A.E. Synthesis of precipitated calcium carbonate: A review. *Carbonates Evaporites* **2018**, *33*, 331–346. [CrossRef]
11. Wen, Y.; Xiang, L.; Jin, Y. Synthesis of plate-like calcium carbonate via carbonation route. *Mater. Lett.* **2003**, *57*, 2565–2571. [CrossRef]
12. Doelle, K.; Amaya, J.J. Application of calcium carbonate for uncoated digital printing paper from 100% eucalyptus pulp. *Tappi J.* **2012**, *11*, 51–59. [CrossRef]
13. Han, J.S.; Jung, S.Y.; Kang, D.S.; Seo, Y.B. Development of flexible calcium carbonate for papermaking filler. *ACS Sustain. Chem. Eng.* **2020**, *8*, 8994–9001. [CrossRef]
14. Wang, J.; Wei, P.; Liu, P.; Sun, W. Identifying appropriate conditions for producing spindle-like causticizing precipitated calcium carbonate for paper filler applications. *BioResources* **2012**, *7*, 5894–5903. [CrossRef]
15. Karakaş, F.; Hassas, B.V.; Celik, M.S. Effect of precipitated calcium carbonate additions on waterborne paints at different pigment volume concentrations. *Prog. Org. Coat.* **2015**, *83*, 64–70. [CrossRef]
16. Mori, Y.; Isogai, A.; Enomae, T. Application of vaterite-type calcium carbonate prepared by ultrasound for ink jet paper. *J. Imaging Sci. Technol.* **2010**, *54*, 020504–020504-6. [CrossRef]
17. Mohamed, M.; Yusup, S.; Maitra, S. Decomposition study of calcium carbonate in cockle shell. *J. Eng. Sci. Technol.* **2012**, *7*, 1–10.
18. Wenyu, S.; Qingfeng, L.; Enguang, H.; Shoutian, C. Study on properties of polymers packed by aragonite whisker. In Proceedings of the 6th International Conference on Properties and Applications of Dielectric Materials (Cat. No. 00CH36347), Xi'an, China, 21–26 June 2000; IEEE: Piscataway, NJ, USA; pp. 431–434.
19. Saulat, H.; Cao, M.; Khan, M.M.; Khan, M.; Khan, M.M.; Rehman, A. Preparation and applications of calcium carbonate whisker with a special focus on construction materials. *Constr. Build. Mater.* **2020**, *236*, 117613. [CrossRef]
20. Ohgushi, H.; Okumura, M.; Yoshikawa, T.; Inboue, K.; Senpuku, N.; Tamai, S.; Shors, E.C. Bone formation processin porous calcium carbonate and hydroxyapatite. *J. Biomed. Mater. Res.* **1992**, *26*, 885–895. [CrossRef]
21. Tolba, E.; Müller, W.E.; Abd El-Hady, B.M.; Neufurth, M.; Wurm, F.; Wang, S.; Schröder, H.C.; Wang, X. High biocompatibility and improved osteogenic potential of amorphous calcium carbonate/vaterite. *J. Mater. Chem. B* **2016**, *4*, 376–386. [CrossRef]
22. Ramakrishna, C.; Thenepalli, T.; Ahn, J.W. Evaluation of various synthesis methods for calcite-precipitated calcium carbonate (PCC) formation. *Korean Chem. Eng. Res.* **2017**, *55*, 279–286.
23. Vikulina, A.; Voronin, D.; Fakhrullin, R.; Vinokurov, V.; Volodkin, D. Naturally derived nano-and micro-drug delivery vehicles: Halloysite, vaterite and nanocellulose. *New J. Chem.* **2020**, *44*, 5638–5655. [CrossRef]
24. Hubbe, M.A.; Gill, R.A. Fillers for papermaking: A review of their properties, usage practices, and their mechanistic role. *BioResources* **2016**, *11*, 2886–2963. [CrossRef]
25. Tai, C.Y.; Chen, F.B. Polymorphism of $CaCO_3$, precipitated in a constant—Composition environment. *AIChE J.* **1998**, *44*, 1790–1798. [CrossRef]
26. Brečević, L.; Kralj, D. On calcium carbonates: From fundamental research to application. *Croat. Chem. Acta* **2007**, *80*, 467–484.
27. Xie, A.-J.; Shen, Y.-H.; Zhang, C.-Y.; Yuan, Z.-W.; Zhu, X.-M.; Yang, Y.-M. Crystal growth of calcium carbonate with various morphologies in different amino acid systems. *J. Cryst. Growth* **2005**, *285*, 436–443. [CrossRef]
28. Becker, A.; Ziegler, A.; Epple, M. The mineral phase in the cuticles of two species of Crustacea consists of magnesium calcite, amorphous calcium carbonate, and amorphous calcium phosphate. *Dalton Trans.* **2005**, *2005*, 1814–1820. [CrossRef]
29. Toffolo, M.B. The significance of aragonite in the interpretation of the microscopic archaeological record. *Geoarchaeology* **2021**, *36*, 149–169. [CrossRef]
30. Demichelis, R.; Raiteri, P.; Gale, J.D.; Dovesi, R. The multiple structures of vaterite. *Cryst. Growth Des.* **2013**, *13*, 2247–2251. [CrossRef]
31. Friedman, G.; Schultz, D. Precipitation of vaterite ($CaCO_3$) during oil field drilling. *Mineral. Mag.* **1994**, *58*, 401–408. [CrossRef]
32. Park, W.K.; Ko, S.-J.; Lee, S.W.; Cho, K.-H.; Ahn, J.-W.; Han, C. Effects of magnesium chloride and organic additives on the synthesis of aragonite precipitated calcium carbonate. *J. Cryst. Growth* **2008**, *310*, 2593–2601. [CrossRef]
33. Zhang, Z.; Xie, Y.; Xu, X.; Pan, H.; Tang, R. Transformation of amorphous calcium carbonate into aragonite. *J. Cryst. Growth* **2012**, *343*, 62–67. [CrossRef]
34. Xiang, L.; Xiang, Y.; Wang, Z.; Jin, Y. Influence of chemical additives on the formation of super-fine calcium carbonate. *Powder Technol.* **2002**, *126*, 129–133. [CrossRef]
35. Yu, J.; Lei, M.; Cheng, B.; Zhao, X. Effects of PAA additive and temperature on morphology of calcium carbonate particles. *J. Solid State Chem.* **2004**, *177*, 681–689. [CrossRef]
36. Lam, R.S.; Charnock, J.M.; Lennie, A.; Meldrum, F.C. Synthesis-dependant structural variations in amorphous calcium carbonate. *CrystEngComm* **2007**, *9*, 1226–1236. [CrossRef]
37. Isopescu, R.; Mateescu, C.; Mihai, M.; Dabija, G. The effects of organic additives on induction time and characteristics of precipitated calcium carbonate. *Chem. Eng. Res. Des.* **2010**, *88*, 1450–1454. [CrossRef]
38. Meldrum, F. Calcium carbonate in biomineralisation and biomimetic chemistry. *Int. Mater. Rev.* **2003**, *48*, 187–224. [CrossRef]
39. Parakhonskiy, B.V.; Haase, A.; Antolini, R. Sub-micrometer vaterite containers: Synthesis, substance loading, and release. *Angew. Chem.* **2012**, *124*, 1221–1223. [CrossRef]

40. Trushina, D.B.; Bukreeva, T.V.; Antipina, M.N. Size-controlled synthesis of vaterite calcium carbonate by the mixing method: Aiming for nanosized particles. *Cryst. Growth Des.* **2016**, *16*, 1311–1319. [CrossRef]
41. Flaten, E.M.; Seiersten, M.; Andreassen, J.-P. Polymorphism and morphology of calcium carbonate precipitated in mixed solvents of ethylene glycol and water. *J. Cryst. Growth* **2009**, *311*, 3533–3538. [CrossRef]
42. Svenskaya, Y.I.; Fattah, H.; Inozemtseva, O.A.; Ivanova, A.G.; Shtykov, S.N.; Gorin, D.A.; Parakhonskiy, B.V. Key parameters for size-and shape-controlled synthesis of vaterite particles. *Cryst. Growth Des.* **2018**, *18*, 331–337. [CrossRef]
43. Chawla, J.S.; Amiji, M.M. Biodegradable poly (ε-caprolactone) nanoparticles for tumor-targeted delivery of tamoxifen. *Int. J. Pharm.* **2002**, *249*, 127–138. [CrossRef] [PubMed]
44. Trushina, D.B.; Borodina, T.N.; Belyakov, S.; Antipina, M.N. Calcium carbonate vaterite particles for drug delivery: Advances and challenges. *Mater. Today Adv.* **2022**, *14*, 100214. [CrossRef] [PubMed]
45. *07014*; Calcium Carbonate. Republic of China National Regulations Database Standards: Taipei, Taiwan, 2023.
46. Zhang, Z.; Yang, B.; Tang, H.; Chen, X.; Wang, B. High-yield synthesis of vaterite $CaCO_3$ microspheres in ethanol/water: Structural characterization and formation mechanisms. *J. Mater. Sci.* **2015**, *50*, 5540–5548. [CrossRef]
47. Devos, C.; Van Gerven, T.; Kuhn, S. A review of experimental methods for nucleation rate determination in large-volume batch and microfluidic crystallization. *Cryst. Growth Des.* **2021**, *21*, 2541–2565. [CrossRef]
48. Tamam, H.; Park, J.; Gadalla, H.H.; Masters, A.R.; Abdel-Aleem, J.A.; Abdelrahman, S.I.; Abdelrahman, A.A.; Lyle, L.T.; Yeo, Y. Development of liposomal gemcitabine with high drug loading capacity. *Mol. Pharm.* **2019**, *16*, 2858–2871. [CrossRef]
49. Donatan, S.; Yashchenok, A.; Khan, N.; Parakhonskiy, B.; Cocquyt, M.; Pinchasik, B.-E.; Khalenkow, D.; Möhwald, H.; Konrad, M.; Skirtach, A. Loading capacity versus enzyme activity in anisotropic and spherical calcium carbonate microparticles. *ACS Appl. Mater. Interfaces* **2016**, *8*, 14284–14292. [CrossRef]
50. Volodkin, D.V.; Petrov, A.I.; Prevot, M.; Sukhorukov, G.B. Matrix polyelectrolyte microcapsules: New system for macromolecule encapsulation. *Langmuir* **2004**, *20*, 3398–3406. [CrossRef] [PubMed]
51. Flaten, E.M.; Seiersten, M.; Andreassen, J.-P. Growth of the calcium carbonate polymorph vaterite in mixtures of water and ethylene glycol at conditions of gas processing. *J. Cryst. Growth* **2010**, *312*, 953–960. [CrossRef]